ESSOAr | https://doi.org/10.1002/essoar.10502174.1 | Non-exclusive | First posted online: Fri, 7 Feb 2020 06:51:43 | This content has not been peer reviewed.

Tectonic inheritance from deformation fabric in the brittle and ductile southern California crust

Vera Schulte-Pelkum[1,2], Zachary E. Ross[3], Karl Mueller[2], Yehuda Ben-Zion[4]

[1]Cooperative Institute for Research in Environmental Sciences (CIRES), University of Colorado, Boulder, Colorado, USA

[2]Department of Geological Sciences, University of Colorado, Boulder, Colorado, USA

[3]Seismological Laboratory, California Institute of Technology, Pasadena, California, USA

[4]Department of Earth Sciences, University of Southern California, Los Angeles, USA

Key Points:

- Receiver function harmonic conversions show pervasive dipping lithospheric fabric in Southern California
- Seismicity is listric near the brittle-ductile transition on profiles across major transform faults
- Non-optimal dipping fault geometry for strike-slip motion is likely due to tectonic inheritance

Corresponding author: Vera Schulte-Pelkum, vera.schulte-pelkum@colorado.edu

ESSOAr | https://doi.org/10.1002/essoar.10502174.1 | Non-exclusive | First posted online: Fri, 7 Feb 2020 06:51:43 | This content has not been peer reviewed.

Abstract

Plate motions in Southern California have undergone a transition from compressional and extensional regimes to a dominantly strike-slip regime in the Miocene. Strike-slip motion is most easily accommodated on vertical faults, and major transform fault strands in the region are typically mapped as near-vertical on the surface. However, some previous work suggests these faults have a dipping or listric geometry at depth. We analyze receiver function arrivals that vary harmonically with backazimuth at all available broadband stations in the region. The results show a dominant signal from contrasts in dipping foliation as well as dipping isotropic contrasts from all crustal depths, including from the ductile middle to lower crust. We interpret these receiver function observations as a dipping fault-parallel structural fabric that is pervasive throughout the region. The strike of these structures and fabrics is parallel to that of nearby fault surface traces. We also plot microseismicity on depth profiles perpendicular to major strike-slip faults and find consistently NE-dipping lineations in seismicity shallowing in dip from near vertical (80-85°) on the Elsinore Fault near the coastal ranges to 60-65° slightly further inland on the San Jacinto Fault to 50-55° on the San Andreas Fault. Taken together, the dipping features in seismicity and in rock fabric suggest that preexisting fabrics and faults likely act as strain guides in the modern slip regime, with reactivation-like mechanisms operating both above and below the brittle-ductile transition.

1 Introduction

The San Andreas Fault (SAF) is the main strand of the California plate boundary between the Pacific and North American plates. In central California, strike-slip motion is focused on the SAF, and observations of deep seismicity and tremor in the lower crust suggest a vertical fault structure cutting through the entire crust (Becken, Ritter, Bedrosian, & Weckmann, 2011; Johnson, Shelly, & Bradley, 2013; Nadeau & Dolenc, 2005; Ryberg, Haberland, Fuis, Ellsworth, & Shelly, 2010; Shelly, 2017; Shelly & Hardebeck, n.d.). The fault geometry in Southern California is considerably more complex, with a long restraining bend in the SAF south of which strain is partitioned onto several major strike-slip faults along with thrust an normal structures in the region. The main additional active strike-slip faults include the San Jacinto Fault (SJF) and Elsinore Fault (EF) lying between the SAF and the coast to the southwest. The subsurface geometry of strike-slip faults including the SAF is generally treated as vertical (e.g., Plesch et al.,

ESSOAr | https://doi.org/10.1002/essoar.10502174.1 | Non-exclusive | First posted online: Fri, 7 Feb 2020 06:51:43 | This content has not been peer reviewed.

2007), but recent work proposed dipping or listric geometry at depth along most of the SAF (Barak, Klemperer, & Lawrence, 2015; Fuis et al., 2017; Fuis, Scheirer, Langenheim, & Kohler, 2012; Qiu, Lin, & Ben-Zion, 2019; Share, Guo, Thurber, Zhang, & Ben-Zion, 2019) and for parts of the SJF (Ross, Hauksson, & Ben-Zion, 2017), with all dips to the northeast except for a SW-dipping segment just south of the central SAF (Fuis et al., 2012).

Nonvertical geometries of strike-slip faults are of interest because ground shaking is increased on the hanging wall compared to a vertical geometry (Fuis et al., 2017; Oglesby, Archuleta, & Nielsen, 2000). Such geometries may contain information on older fault networks that may influence present day deformation behavior. They may also affect the interpretation of geodetic data (e.g., Dair & Cooke, 2009; Fialko, 2006; Lindsey & Fialko, 2013). Development of a nonvertical strike-slip fault has previously been interpreted as recording the reactivation of a prior dipping thrust or normal fault (Avouac et al., 2014; Sato, Kato, Abe, Van Horne, & Takeda, 2015). Dipping geometries on the SJF and EF have also been suggested as a consequence of inheritance from the shallowly dipping Western Salton Detachment fault (Dorsey, Axen, Peryam, & Kairouz, 2012; Mason et al., 2017). Inheritance of preexisting faults from past deformation regimes can influence the evolution of faults tha accommodate strain in response to a change in plate motion, here related to subduction of an oceanic spreading ridge (Atwater & Stock, 1998). Inheritance and reactivation can also be related to older rock fabrics or rheological boundaries such as the edges of batholiths. Dip on the SAF may be due to fault localization along the boundary of a previously underthrust mafic Pacific plate under the North American plate in the region of the San Gorgonio to Cajon passes and southern SAF (Barak et al., 2015; Fuis et al., 2017).

An additional open question is how faults root and are connected between the brittle crust and the ductile lower crust and lithospheric mantle. It is unknown whether major continental transform faults root into localized subvertical shear zones, coalesce into wider regional-scale shear zones, or root into an evenly shared ductile substrate (Bernard & Behr, 2017; Sibson, 1983; Titus, Medaris, Wang, & Tikoff, 2007). As in the brittle case, if earlier strain led to fabric development in the ductile lithosphere, such inherited ductile fabric may lead to mechanical anisotropy and change the deformation response to applied stress. It is unknown how quickly plastic lithospheric fabric may be reset under a new stress field (Vauchez, Tommasi, & Mainprice, 2012). Ductile crustal and lithospheric

ESSOAr | https://doi.org/10.1002/essoar.10502174.1 | Non-exclusive | First posted online: Fri, 7 Feb 2020 06:51:43 | This content has not been peer reviewed.

fabric and shear zone geometry may in turn affect how faults are loaded at brittle depths (e.g. Bourne, England, & Parsons, 1998; Dolan, Bowman, & Sammis, 2007; England & Jackson, 1989; Montési, 2004; Platt & Becker, 2010; Roy & Royden, 2000a, 2000b). Fault geometries near the brittle-ductile transition and deformation fabric at ductile depths are therefore of particular interest.

Our goal in this study is to investigate the geometry of faults and of shear zones and rock fabric below faults in Southern California using two types of data. The first data set consists of azimuthally varying arrivals in receiver functions that are generated from contrasts in dipping shear fabric or dipping isotropic interfaces (section 2). Previous anisotropic receiver function work focused on the lower crust (Porter, Zandt, & McQuarrie, 2011) and on integrated shear fabric throughout the crust and uppermost mantle (Schulte-Pelkum & Mahan, 2014b) at a selected number of permanent stations. We present depth-dependent results throughout the lithosphere at all available permanent and temporary broadband stations. The second data set is the waveform-based, relocated Southern California catalog of relocations for 1981-2017 by Hauksson, Yang, and Shearer (2012). We plot profiles showing the fine structure of seismicity across major fault strands and near the brittle-ductile transition in section 2. We synthesize the findings from seismicity and receiver function anisotropy in terms of tectonics, geodynamic memory, and the influence of geological history on present-day deformation via inheritance of faults and fabrics in section 4.

2 Receiver function arrivals from anisotropic and dipping contrasts

Previous work using receiver functions in Southern California based on a sparser subset of stations suggested dipping foliation in the lower crust (Porter et al., 2011) and in the entire lithosphere (Schulte-Pelkum & Mahan, 2014b). If present day strike-slip motion controls lithospheric fabric, one might expect vertical faults and vertical shear planes in this region rather than dipping ones. Crustal layers with vertical foliation or horizontal lineation generate receiver function arrivals with π-periodic polarity (second azimuthal harmonic, A_2) changes in backazimuth (Brownlee et al., 2017; Levin & Park, 1998). In surface wave studies, such fabric is referred to as having azimuthal anisotropy (e.g. Lin, Ritzwoller, Yang, Moschetti, & Fouch, 2011). Figure 1 displays which stations in the EarthScope Transportable Array show at least one A_2-periodic arrival with an amplitude exceeding 10% horizontal to vertical amplitude ratio within the first 8 seconds

ESSOAr | https://doi.org/10.1002/essoar.10502174.1 | Non-exclusive | First posted online: Fri, 7 Feb 2020 06:51:43 | This content has not been peer reviewed.

(lithospheric depths), requiring a lithospheric layer with strong vertical foliation or horizontal lineation (Schulte-Pelkum & Mahan, 2014b). A strong A_2 signal is plotted as a station with a cross. The cross bars denote the fast and slow orientation of anisotropy averaged over depths exceeding 10% signal amplitude, which are degenerate in this analysis unless additional assumptions are made. The A_2 signal dominates in the northern Basin and Range and the coastal ranges of Central California, while it is weak (stations without crosses) in the Snake River Plain, the Colorado Plateau, the southern Basin and Range, and the Sierra Nevada (Figure 1). Since the transform plate boundary runs through Southern California into the Central California coastal ranges, it is surprising that Southern California shows a weaker azimuthal anisotropy signal than the latter region. Previous studies (Porter et al., 2011; Schulte-Pelkum & Mahan, 2014b) also suggest dominant dipping rather than vertical foliation in Southern California. In the present study, we analyze all available permanent and temporary stations from 2004-2017, forming a denser data set, for signatures of contrasts in dipping foliation and dipping isotropic contrasts in receiver functions.

2.1 Receiver function sensitivity to anisotropic and dipping contrasts

Seismic anisotropy is expressed in receiver functions in two fundamentally different ways. One is the splitting of an S arrival after conversion from P; the most commonly used is the P-to-S conversion from the Moho. We do not apply this method here, as it only provides an integrated measure of anisotropy over the travel path; it is therefore unlikely to accurately measure anisotropy from shear zones with limited thickness, and may also not provide an accurate measure of bulk crustal anisotropy because of arrivals from thin anisotropic layers masquerading as bulk volume splitting (Liu & Park, 2017).

A more appropriate method in the presence of intracrustal anisotropic structure uses the azimuthally varying conversion from a contrast in anisotropy (Figure 2). A contrast in anisotropy of about 3% or a change in foliation orientation are sufficient to generate large-amplitude arrivals comparable to those from an average isotropic Moho contrast (Schulte-Pelkum & Mahan, 2014a). The conversions from such a contrast display characteristic polarity reversals with backazimuth on transverse as well as radial components (C. Jones & Phinney, 1998; Park & Levin, 2016; Savage, 1998; Schulte-Pelkum & Mahan, 2014a). The depth of such a contrast is given by the arrival time of the conversion in the receiver function (Figure 2), giving this method depth resolution, unlike

ESSOAr | https://doi.org/10.1002/essoar.10502174.1 | Non-exclusive | First posted online: Fri, 7 Feb 2020 06:51:43 | This content has not been peer reviewed.

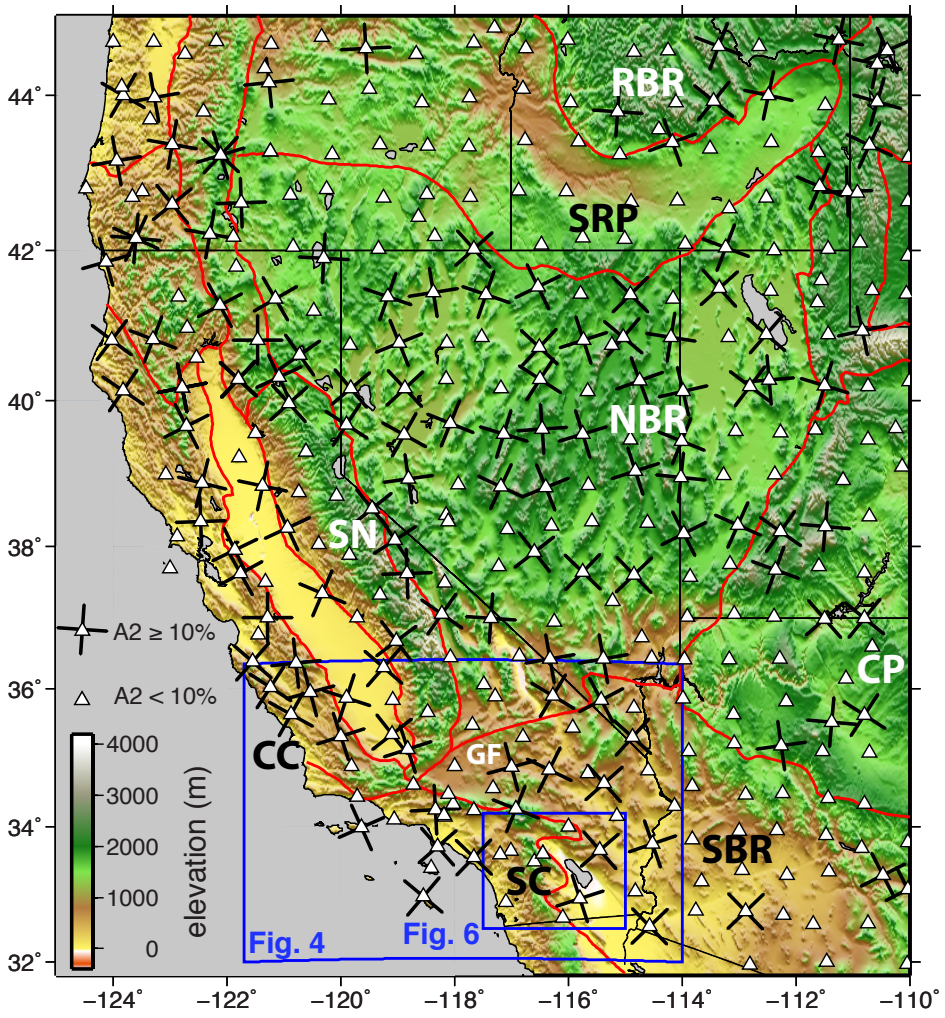

Figure 1. Map of stations in the EarthScope Transportable Array (white triangles) where the A_2-periodic azimuthal signal from anisotropy exceeds (black bars) or does exceed (triangle without bars) 10% of the receiver function amplitude. Black bars are fast and slow orientations averaged axially over the parts of the signal exceeding 10%. Red lines are physiographic province boundaries. Blue lines show extents of later figures. RBR-Rocky Mountain Basin and Range; SRP-Snake River Plain; NBR-Northern Basin and Range; SN-Sierra Nevada; CP-Colorado Plateau; CC-Central California; GF-Garlock Fault; SBR-Southern Basin and Range; SC-Southern California. Analysis details in Schulte-Pelkum and Mahan (2014b).

splitting methods. Thin shear layers can also be resolved as long as conversions from the top and bottom of the layer are separated by close to a pulse width of the receiver function (usually 2-3 km thickness for receiver functions calculated at 1 Hz or higher). In

ESSOAr | https://doi.org/10.1002/essoar.10502174.1 | Non-exclusive | First posted online: Fri, 7 Feb 2020 06:51:43 | This content has not been peer reviewed.

many previous studies, arrivals are modeled directly to arrive at a usually nonunique model of anisotropy (Ozacar & Zandt, 2009; Porter et al., 2011; Vergne, Wittlinger, Farra, & Su, 2003; Zandt et al., 2004). However, the harmonic behavior can be exploited directly (without forward modeling) to systematically separate signal from azimuthal anisotropy (horizontal symmetry axis) in the π-periodic amplitude component (A_2) and dipping foliation (plunging symmetry axis) in the 2π-symmetric component (A_1; Bianchi, Park, Agostinetti, & Levin, 2010; Bianchi, Piana Agostinetti, De Gori, & Chiarabba, 2008; Brownlee et al., 2017; Liu & Park, 2017; Long, Ford, Abrahams, & Wirth, 2017; Schulte-Pelkum & Mahan, 2014b). Some studies focus on azimuthal anisotropy using the A_2 component because of an argument that the A_1 component is also sensitive to dipping isotropic contrasts (Savage, 1998). However, the sensitivity to plunging axis anisotropy is much higher than for horizontal axis anisotropy (Park & Levin, 2016; Schulte-Pelkum & Mahan, 2014b). The method used here solves for strike of a dipping isotropic contrast or strike of the plane perpendicular to the symmetry axis of anisotropy, whether that is a slow or fast axis (Figure 2). This strike and the depth of the contrast in velocity or anisotropy are the most robust observables (Schulte-Pelkum & Mahan, 2014a, 2014b). The sense of dip trades off with whether the anisotropy is best approximated by a fast or slow symmetry axis, and if the stronger anisotropy is above or below the interface (Figure 2). The amplitude of the A_1 arrival depends on the strength of the anisotropic or isotropic contrast as well as on the plunge of the symmetry axis or the isotropic contrast dip, with intermediate foliation dips generating larger conversion amplitudes than subhorizontal or subvertical foliation in the anisotropic case (Brownlee et al., 2017).

Figure 2 illustrates how strikes of isotropic dip and of shear fabric foliation resulting from geological deformation processes are similar in orientation, such that the distinction between isotropic dip and dipping foliation contrast becomes are secondary question. A distinction between a contrast plunging axis anisotropy at depth versus an isotropic dipping interface can be made by the fact that a polarity-reversed arrival is seen at zero time in the isotropic dip case (Schulte-Pelkum & Mahan, 2014b).

2.2 Data and analysis

We analyze broadband data from stations of the USArray, Southern California Seismic Network (SCSN), and Anza networks for the years 2004-2017, as well as from the 1997-1998 LARSE II experiment (Murphy et al., 2010; Zhu, 2002) and 2011 Salton Seis-

ESSOAr | https://doi.org/10.1002/essoar.10502174.1 | Non-exclusive | First posted online: Fri, 7 Feb 2020 06:51:43 | This content has not been peer reviewed.

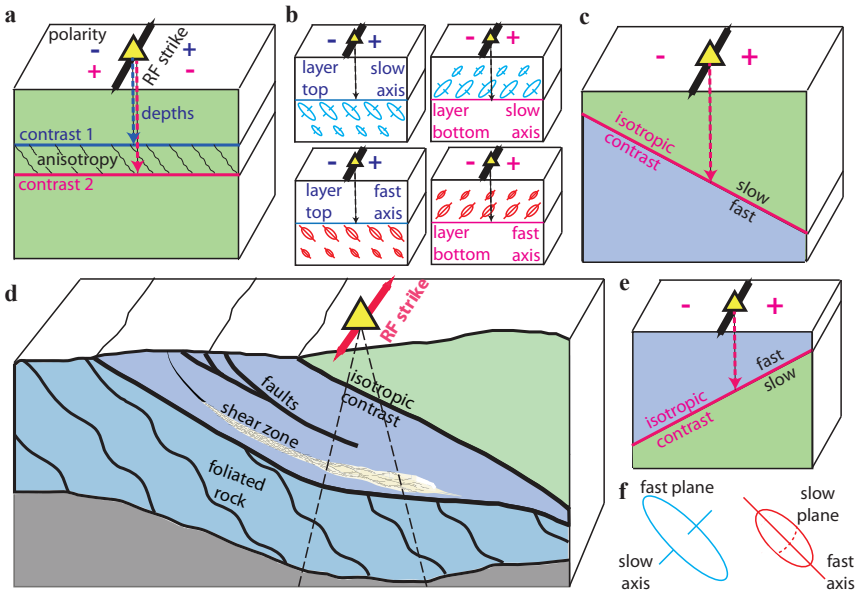

Figure 2. Illustration of sensitivity of receiver function to deformation-related structures in the lithosphere. (a) Horizontal layer with anisotropy (dipping foliation with fast Vp planes shown as wavy lines) embedded in isotropic layer with same average velocity (no isotropic velocity contrast). Receiver functions from different backazimuths at station (yellow triangle) show two arrivals with opposite polarity (+ and - signs) indicating foliation strike shown as black bar, one at a delay time corresponding to the depth of the blue contrast (blue dashed arrow), another from depth of the red contrast (red dashed arrow). (b) Illustration of tradeoffs between sense of foliation dip, anisotropic symmetry (fast- or slow-axis symmetry approximation), and whether an arrival is generated at the top or bottom of a layer with stronger anisotropy, with symbols explained in f. All four cases generate the same polarity reversal pattern. (c) Dipping interface with contrast in isotropic Vs; black bar is strike registered at station, depth of red interface below station is found via delay time as in the anisotropic case. (d) Conceptual tectonic sketch after Fossen and Cavalcante (2017) and Harms et al. (2004) showing a composite of cases (a) and (b) within a compressional setting: Isotropic contrasts across faults (black lines), localized shear zone (beige), and distributed shear fabric (purple) with strike of these features picked up by receiver functions at station (yellow) from several depths; dashed lines show receiver function sampling cone. (e) Illustration of tradeoff in dip sense in the isotropic contrast case; this case generates the same polarity pattern as case c. (f) Explanation of symbols used in b.

mic Imaging Project (Barak et al., 2015). In order to maximize azimuthal coverage, we calculate receiver functions for P and P_{diff} arrivals from 30-150° epicentral distance for

ESSOAr | https://doi.org/10.1002/essoar.10502174.1 | Non-exclusive | First posted online: Fri, 7 Feb 2020 06:51:43 | This content has not been peer reviewed.

all events with magnitude 5.0 and larger and apply an automated selection and quality control process (Schulte-Pelkum & Mahan, 2014b). From all events, we retain a mean of 6% of radial and 3% of the transverse component receiver functions with high signal-to-noise ratios and stable deconvolutions. We use the time domain algorithm by Ligoria and Ammon (1999) and a Gaussian filter factor of 3. Details of the processing and quality control methods are as in Schulte-Pelkum and Mahan (2014b).

The harmonic behavior is described in Schulte-Pelkum and Mahan (2014a) and the analysis method in Schulte-Pelkum and Mahan (2014b); we summarize it briefly here using station LPC near Cajon Pass as an example (Figure 3). After calculating radial and transverse component receiver functions, we apply slowness corrections so that the arrival times correspond to vertical incidence and amplitudes to a common incidence angle (C. Jones & Phinney, 1998). We then stack radial and transverse components separately in azimuthal 10° bins (Figure 3a and b). The radial component is a superposition of the isotropic flat-layered signal (termed R_0) that has no variation with backazimuth plus an azimuthally varying portion. We calculate the average radial receiver function over all bins as a proxy for R_0 and subtract it from each bin, so that the azimuthally varying signal remains ($R-R_0$; Figure 3c). Assuming hexagonal symmetry (usually valid for crustal materials; Brownlee et al., 2017), in the case of plunging axis anisotropy the $R-R_0$ component will be the same as the transverse component (T) shifted by 90° clockwise in backazimuth ($\phi-90°$) as shown in Figure 3d; in the horizontal symmetry axis case, the azimuthal shift is 45° (Levin & Park, 1998; Schulte-Pelkum & Mahan, 2014b). To find the plunging axis anisotropy and isotropic dip signal, we stack $R-R_0$ and $T(\phi-90°)$ together in backazimuthal bins (Figure 3e). For all stations with azimuthal gaps smaller than 90°, we apply a moving window of 0.25 s length and solve for the first azimuthal harmonic in amplitude for each time window to obtain an A_1 signal amplitude and phase (Figure 3e, g). The phase of an amplitude peak is perpendicular to the strike of the dipping foliation contrast or dipping isotropic interface (Schulte-Pelkum & Mahan, 2014a, 2014b). The depth of the contrast is obtained by scaling the arrival time in the receiver function to depth using a Vp and Vs model between the converter and station.

In this study, we use the 3-D Southern California Earthquake Center (SCEC) Community Velocity Model CFM-H (Shaw et al., 2015). The largest amplitude arrival at station LPC is at 1.6 s, with an amplitude of 0.2. Amplitudes in time-domain receiver func-

ESSOAr | https://doi.org/10.1002/essoar.10502174.1 | Non-exclusive | First posted online: Fri, 7 Feb 2020 06:51:43 | This content has not been peer reviewed.

tions are absolute ratios of horizontal to vertical component amplitude, and 0.2-0.3 is the range of a strong Moho arrival amplitude. The strike of this arrival is 114° (green dots in Figure 3e), parallel to the strike of the San Andreas Fault beneath the station (Figure 4c). The delay time of 1.6 s results in a depth of the contrast of 12.1 km when migrated with the 3-D velocity model profile at the station location. Figure 3f shows a simplified geological cross section (Forand, Evans, Janecke, & Jacobs, 2018) based on samples from the nearby Cajon Pass borehole (Figure 4c), surface geology, and shallow active source reflection results. The profile shows pervasive NE-dipping structures. A contrast at 12 km beneath the station may be the downdip extension of a listric geometry of the San Jacinto Fault Zone or possibly connected to a range-bounding thrust fault further southwest (Figure 3f). Other arrivals are less prominent in amplitude (Figure 3g, delay time and strike marked as black circles in Figure 3e) and correspond to depths of 0.5, 30.5, and 70 km, with similar strikes. We focus on the largest arrival at each station as the best determined signal for the remainder of this paper.

2.3 Receiver function results

The amplitude, depth, and strike orientation of inferred foliation or dip from the largest arrival at each station are shown in Figure 4 on a map of the entire study area and two magnified subregions, along with azimuthal histograms of the strikes in each map region. NW strikes dominate the set from the entire area. Given the tradeoffs illustrated in Figure 2, additional assumptions are needed to infer the dominant dip sense. If we assume the signal is from either the top of a layer with dipping foliation with slow symmetry axis (Figure 2a), for instance a schist or gneiss layer (Brownlee et al., 2017), or a dipping slow-over-fast isotropic interface (Figure 2c), then a NW strike would imply a foliation or isotropic contrast dip down to the NE. Larger amplitudes imply a stronger foliation or isotropic velocity contrast, but can also be due to intermediate foliation dip angles which generate conversions with larger ampltiudes than those from contrast with subhorizontal or near-vertical foliation (Brownlee et al., 2017). The dominant NW-SE strike mirrors that of the dominant fault orientation, in particular that of the major transform faults in the region. In the Transverse Ranges (Figure 4, bottom left), fault orientations and receiver functions strikes rotate to E-W. In this region, an assumption of arrivals from the top of a layer with dipping foliation or a slow-over-fast isotropic contrast implies dips to the north, consistent with the geometry of thrust faulting located in the

ESSOAr | https://doi.org/10.1002/essoar.10502174.1 | Non-exclusive | First posted online: Fri, 7 Feb 2020 06:51:43 | This content has not been peer reviewed.

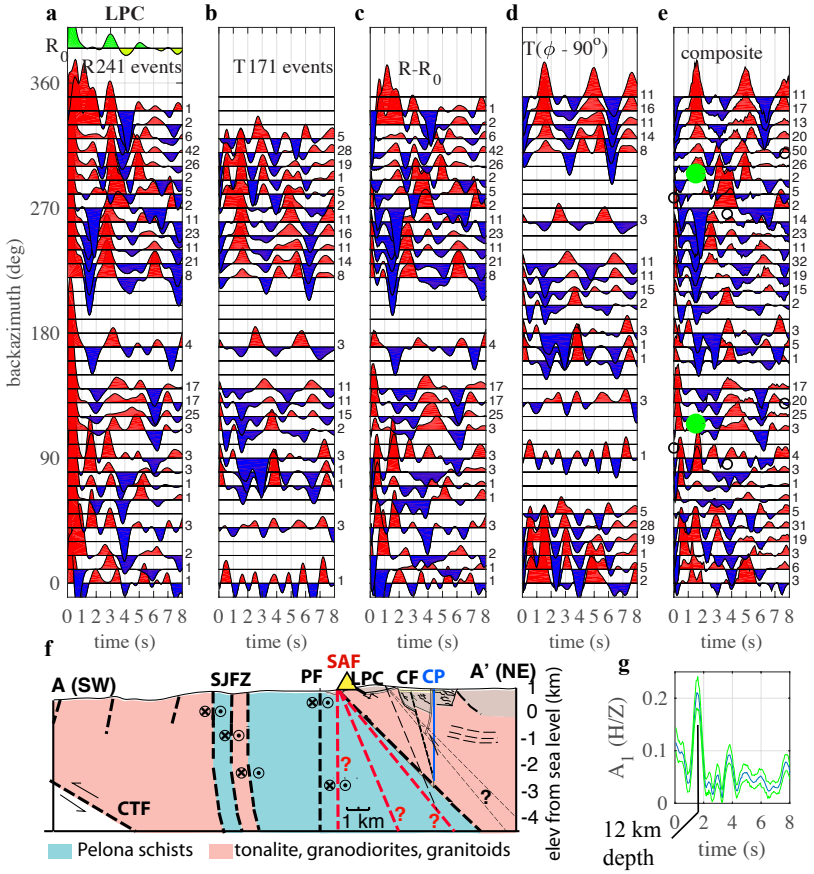

Figure 3. Receiver function analysis for example station LPC near Cajon Pass (Figure 4, bottom right). (a) Radial receiver functions binned by backazimuth after slowness correction; number of events per bin on the right of each trace. Amplitudes are on-normalized, same scale for all subplots. No azimuthal smoothing is applied. Trace on top is average over all azimuthal bins, R_0. (b) Same as a, but transverse component. (c) Radial component after R_0 was subtracted from each bin trace. (d) Transverse component after shifting traces by 90° in backazimuth. (e) Traces from c and d stacked together. Moving window harmonic analysis to determine amplitude and phase of first azimuthal harmonic A_1 is applied to this set (A_1 amplitude shown below in g). Green dots show strike of foliation inferred from maximum arrival, which parallels the SAF trace near the station (Figure 4). Black circles mark strikes of other maxima. (f) Geological cross section simplified from Forand et al. (2018) (profile location in Figure 4), based on Cajon Pass borehole (CP) samples, surface geology, and shallow reflection work. Blue line is borehole, dashed lines are inferred faults, thin dashed lines metamorphic fabric; three alternative proposed dips were drawn by Forand et al. (2018) for SAF. CTF-Cucamonga Thrust Fault; PF-Punchbowl Fault; CF-Cleghorn Fault. (g) A_1 amplitude and 95% confidence interval on same time scale as e.

ESSOAr | https://doi.org/10.1002/essoar.10502174.1 | Non-exclusive | First posted online: Fri, 7 Feb 2020 06:51:43 | This content has not been peer reviewed.

area. In the entire study region, the depths of the contrasts resulting in the largest A_1 arrival at each station are distributed throughout the lithosphere. No systematic changes of strike with depth are apparent.

Figure 5 shows the uncertainty in A_1 amplitude and strike based on bootstrap estimates. Bootstrapping is performed by eliminating azimuthal bins in separate 100 random instances before fitting the A_1 harmonic in each moving window. Azimuthal bin averages rather than individual receiver functions are eliminated to avoid undue weighting of densely sampled backazimuths. The amplitude uncertainty is given as the 95% confidence interval, corresponding to two standard deviations if the distribution is normal. The strike uncertainty is given as the standard error of the strike in the bootstrapped distribution using circular statistics.

Strike uncertainties are small enough that they plot within the strike arrow for all but a few stations (Figure 5). Amplitude uncertainties vary widely and are higher for temporary stations with poorer azimuthal coverage. However, the similarity of results between neighboring stations with smaller and larger nominal uncertainty, for instance in the temporary more densely sampled linear experiments (e.g. the Salton Sea line in the southern part of the study area), suggests that the uncertainties calculated may be unduly pessimistic. We conclude that the receiver functions suggest dominant dipping fabric that is pervasive geographically and throughout the lithosphere in depth, with foliation or dip strikes largely parallel to currently active strike-slip and older inactive thrust or active faults.

3 Seismicity profiles

We compare fault structures as illuminated by microseismicity to the dipping structural fabric imaged at depth using receiver functions by plotting hypocenters on depth profiles perpendicular to major transform faults. We use the entire relocated seismicity catalog of Hauksson et al. (2012), extended to the end of 2017. Figure 6 shows the geographic locations of the earthquakes and of seismicity depth profiles. This analysis covers the southern part of the study area that is dominated by strike-slip faulting, extending just into the big bend area to the north that includes thrust components Yang and Hauksson (2013) for the northernmost profile A-A'. Figure 6 displays prominent geographic trends in the depth of seismicity. The maximum earthquake depth gradually

ESSOAr | https://doi.org/10.1002/essoar.10502174.1 | Non-exclusive | First posted online: Fri, 7 Feb 2020 06:51:43 | This content has not been peer reviewed.

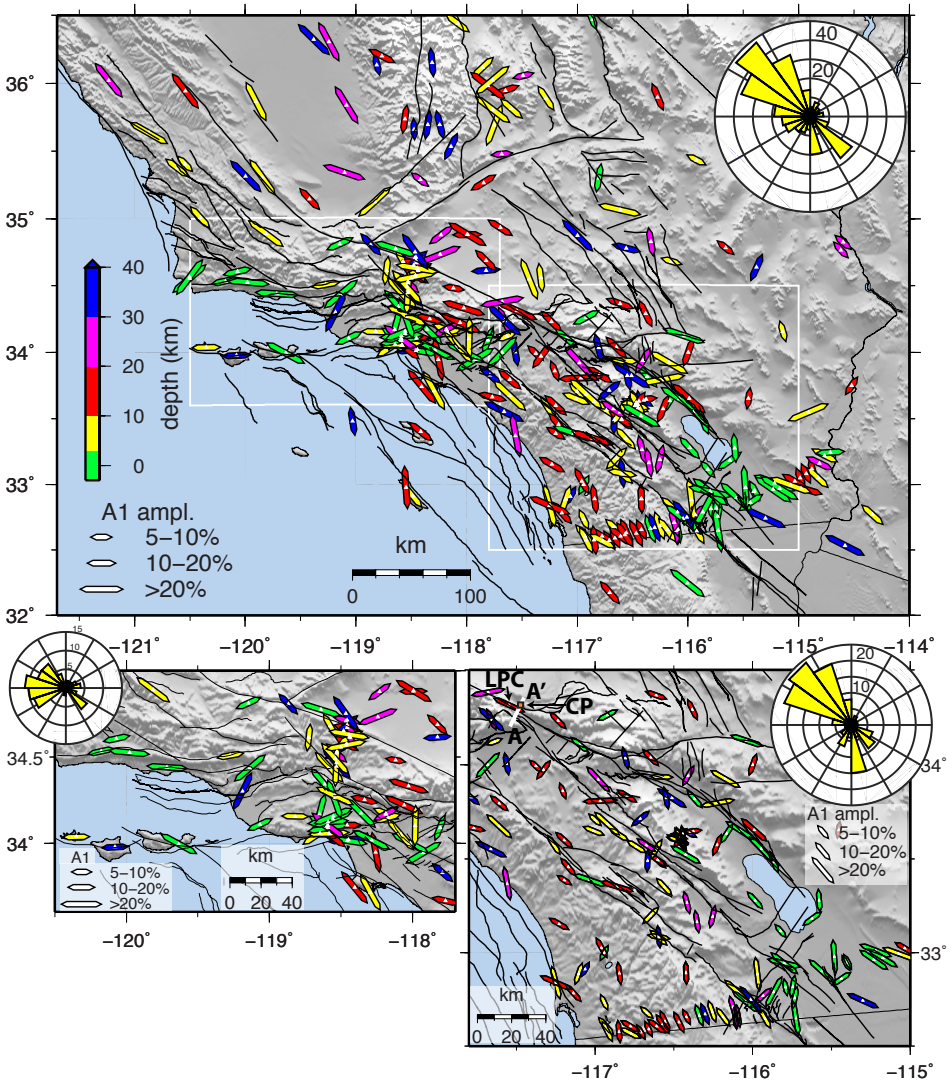

Figure 4. Map showing results for largest A_1 arrival at each station (white dot). See Figure 1 for location. Bar orientation shows the strike of dipping foliation or dipping isotropic interface, length varies with amplitude of the arrival, color indicates depth of the converting contrast. Shading is relief, faults from SCEC CFM-5.2 (Plesch et al., 2007) in black. White outlines are magnified in lower maps. Circular insets are azimuthal histograms of strikes of the bars displayed in each corresponding map (bars on map are shown as axial orientations, while histograms show sense of strike). Numbers in histograms show number of stations in each azimuthal bin. Note the predominance of NW strikes in overall area and in southern SAF - SJFZ - Elsinore Fault area (bottom right) and W strikes in the Transverse Ranges (bottom left). Strikes derived from our analysis are generally parallel those of nearby surface faults (histograms).

ESSOAr | https://doi.org/10.1002/essoar.10502174.1 | Non-exclusive | First posted online: Fri, 7 Feb 2020 06:51:43 | This content has not been peer reviewed.

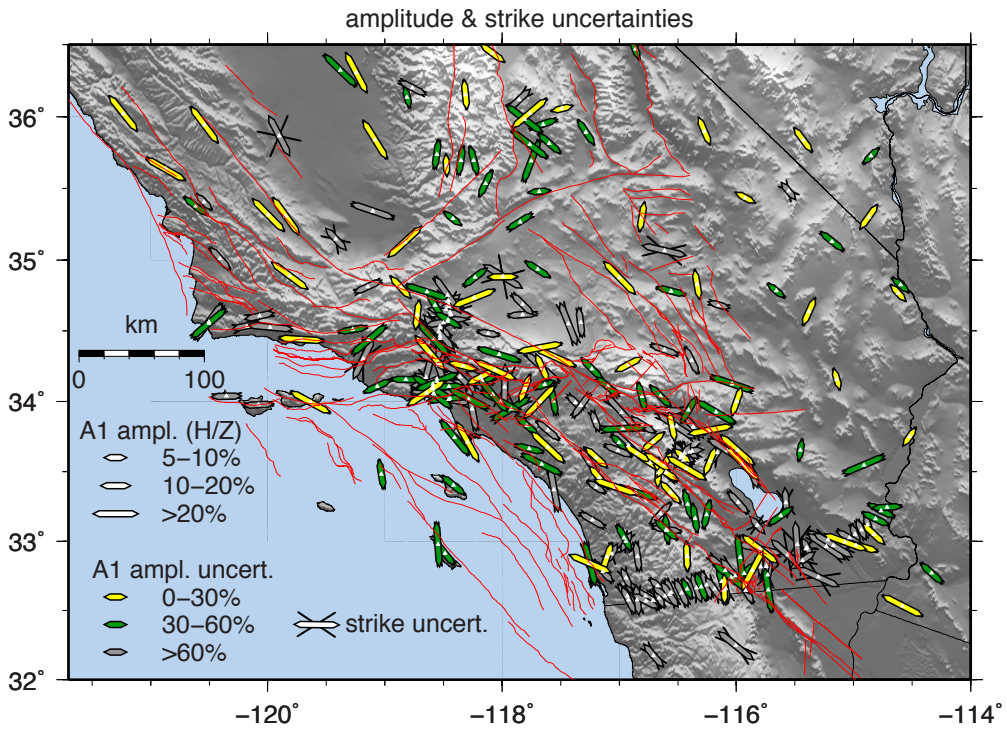

Figure 5. Same as Figure 4, except here color shows amplitude uncertainty based on bootstrap estimation, expressed as percent of the amplitude at each station. Strike uncertainty from bootstrapping is shown as thin grey lines (smaller than width of arrows for most stations).

shallows from 20 km at the northwestern end near the San Jacinto mountains, to 10 km at the southeastern end south of the Salton Sea (supplementary Figure S1). This pattern presumably outlines the brittle-ductile transition, dominantly due to geothermal gradient changes along the profile (Doser & Kanamori, 1986), although other influences on rheology such as composition and shear weakening are also likely (e.g. Hauksson & Meier, 2019; Shinevar, Behn, Hirth, & Jagoutz, 2018).

To better understand the geometry of seismicity across the primary fault zones within the southern California plate boundary area, we examine a set of seismicity profiles roughly perpendicular to the San Andreas, San Jacinto, and Elsinore faults. Figure 7a shows a depth profile of seismicity along the southern SAF (SSAF) using the 1981-2017 SCSN catalog (top subpanel) and 2008-2017 QTM catalog (bottom subpanel). Relocations for the two catalogs were done independently using different methods and velocity models. The SCSN catalog (Hauksson et al., 2012) features a longer time span and captures some

ESSOAr | https://doi.org/10.1002/essoar.10502174.1 | Non-exclusive | First posted online: Fri, 7 Feb 2020 06:51:43 | This content has not been peer reviewed.

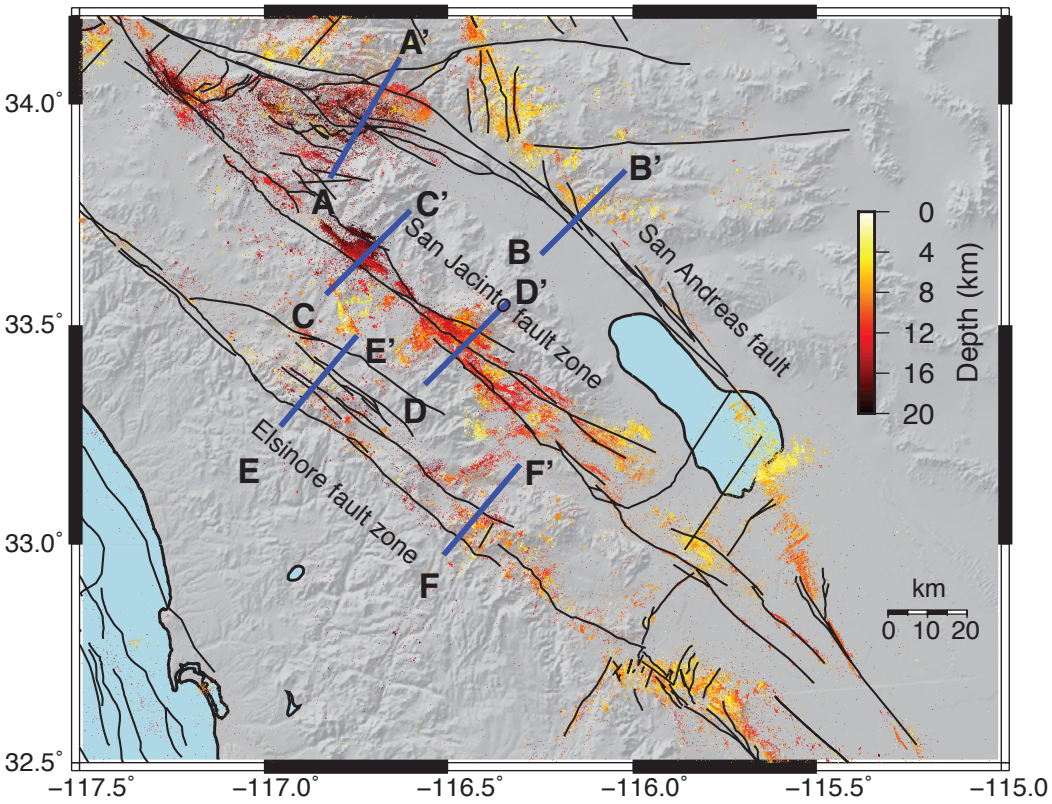

Figure 6. Map of epicenters and seismicity profile locations. Dots are epicenters in SCSN 1981-2017 catalog, color shows hypocenter depth. Relief in greyshade; black lines are fault surface traces from SCEC5 Community Fault Model (CFM, Plesch et al., 2007). Map area is marked in Figure 1 for wider regional context. Blue lines marked A-F are locations of cross-fault depth seismicity profiles in Figure 7.

areas that were quiescent in 2008-2017, while the QTM catalog (Ross, Trugman, Hauksson, & Shearer, 2019) covers a shorter time span but contains magnitudes down to much smaller values (nearly complete for events of magnitude above 0.3, compared to above 1.7 for the SCSN catalog). The vertical projections of the surface traces of the Banning and Mission Creek strands of the SSAF are denoted by the red dashed lines in Figure 7a. Green dashed lines show the average dip of the fault segments according to the SCEC CFM5.2 model. There is a clear northeast dipping structure to the seismicity, with dip values approximately 50-55° over the entire length of the profile. These dip values are close to that of the 1948 M 6.5 Desert Hot Springs (Richter, Allen, & Nordquist, 1958) and 1986 M 6.0 North Palm Springs earthquake (L. Jones, Hutton, Given, & Allen, 1986), which are believed to have occurred on the Mission Creek and Banning Faults, respec-

ESSOAr | https://doi.org/10.1002/essoar.10502174.1 | Non-exclusive | First posted online: Fri, 7 Feb 2020 06:51:43 | This content has not been peer reviewed.

tively. Fuis et al. (2017) argue based on this information and various other data sets and observations that the SSAF in this area as a whole dips 50-60° to the northeast. In addition to these observations, there is a broad area of microseismicity interpreted as the damage zone spanning about 15 km along the profile. A notable feature of this damage zone is that it is asymmetric across the fault. The QTM catalog shows more fine structure as expected from the lower magnitude threshold, while the SCSN catalog show a planar feature predating the QTM catalog in the northeasten portion of the profile.

Moving further to the southeast along the SSAF, Figure 7b shows a depth section which also exhibits a northeast dipping structure to the seismicity. This is consistent with observations of head waves propagating along a dipping bimaterial fault in the region (Share & Ben-Zion, 2016). Here, the fault system has a slightly steeper dip than along profile A-A', and while the seismicity is shallower overall, the damage zone here is fully on the northeast side of the SSAF. A NE-dipping SAF was inferred at this location and south along the Salton Sea by Barak et al. (2015) using surface wave tomography.

Next, we move to the San Jacinto fault zone (SJFZ), which is located to the southwest of the SSAF. Figure 7c contains a seismicity profile (3) across the Clark strand of the SJFZ through the Hot Springs segment. In this area, the seismicity also defines northeast dipping planes, however they dip about 65-70°, compared with the dips of 50-60° observed for the seismicity on the SSAF. The seismicity has a listric appearance, even more so than in profile Figure 7a.

The dipping pattern is also apparent in the complex trifurcation area of the SJFZ, which is located about 40 km to the southeast (Figure 7d). This area was studied in detail by Ross et al. (2017), who noted that in addition to the seismicity, the focal mechanisms at depth showed planes dipping about 70° to the northeast. They further suggested that the SJFZ transitions from dipping to near-vertical above around 8 km depth based on the relative positions of the surface traces of the main faults and steeper focal mechanism and seismicity dips in the shallow structure. As with the SSAF, the damage zones in these areas of the SJFZ are also predominantly located on the northeast side of the surface trace of the fault. Miocene-age structures that are part of the Colorado River extensional corridor (Shirvell, Stockli, Axen, & Grove, 2009) formed low-angle, east-rooting normal faults. One such fault is the Western Salton Detachment (Mason et al., 2017) that is offset by the SAF, SJFZ, and the Elsinore faults from north to south (Dorsey

ESSOAr | https://doi.org/10.1002/essoar.10502174.1 | Non-exclusive | First posted online: Fri, 7 Feb 2020 06:51:43 | This content has not been peer reviewed.

et al., 2012). Mason et al. (2017) propose a transition from NE-dipping shallow normal faulting to more steeply NE-dipping strike-slip motion in the Pleistocene (8 Ma). Pre-existing extensional structures may therefore act as strain guides during subsequent strike-slip faulting.

Finally, we examine two profiles across the Elsinore fault zone (EFZ). While the EFZ has notably less seismicity than the other two faults, the same type of analysis is still possible. Figure 7e and Figure 7f show seismicity profiles across the EFZ which both indicate damage zones containing smaller cracks and faults northeast of the surface fault trace. Figure 7e shows features dipping about 80-85° to the northeast. Figure 7f shows features dipping from vertical to 85° in addition to a subhorizontal to shallowly NE-dipping feature at 3-4 km depth. In both profiles, the damage zone and seismicity are asymmetric to the northeast of the surface trace of the fault. The shallowly dipping feature from 3-4 km depth in profile F matches the position of the Western Salton Detachment fault shown by Dorsey et al. (2012). As in the case of the SJFZ, Dorsey et al. (2012) show a NE dip on the EFZ consistent with synthetic normal faults in the hanging wall of the top-to-the-east Western Salton Detachment system.

The dipping features are unlikely to be artifacts of the relocation procedure because the fabric of the seismicity exhibits these patterns over several different length scales and in both catalogs. These include narrow zones of activity that are relatively isolated, as well as more distributed damage zones that collectively define a persistent dipping pattern. While the relocation procedure performs a cluster analysis to identify which events to group together for relocation, there is no reason that the final locations should collapse to highly-localized seismicity structures. Neither of the relocation methods impose planar features, which gives confidence to the results. The observations are furthermore generally consistent with regional focal mechanisms.

To summarize these results, all three of the major transform fault systems in southern California exhibit narrow planar features of seismicity that dip to the northeast. The dip of each system progressively steepens from about 50° in the northeast to about 80° in the southwest. This steepening may also occur toward the southeast, but the evidence for this is weaker from the seismicity. In addition, the damage zones which produced these earthquakes are all strongly asymmetric across each fault system, with most of the earthquakes occurring on the northeast side. Together, the common patterns for all suggest

ESSOAr | https://doi.org/10.1002/essoar.10502174.1 | Non-exclusive | First posted online: Fri, 7 Feb 2020 06:51:43 | This content has not been peer reviewed.

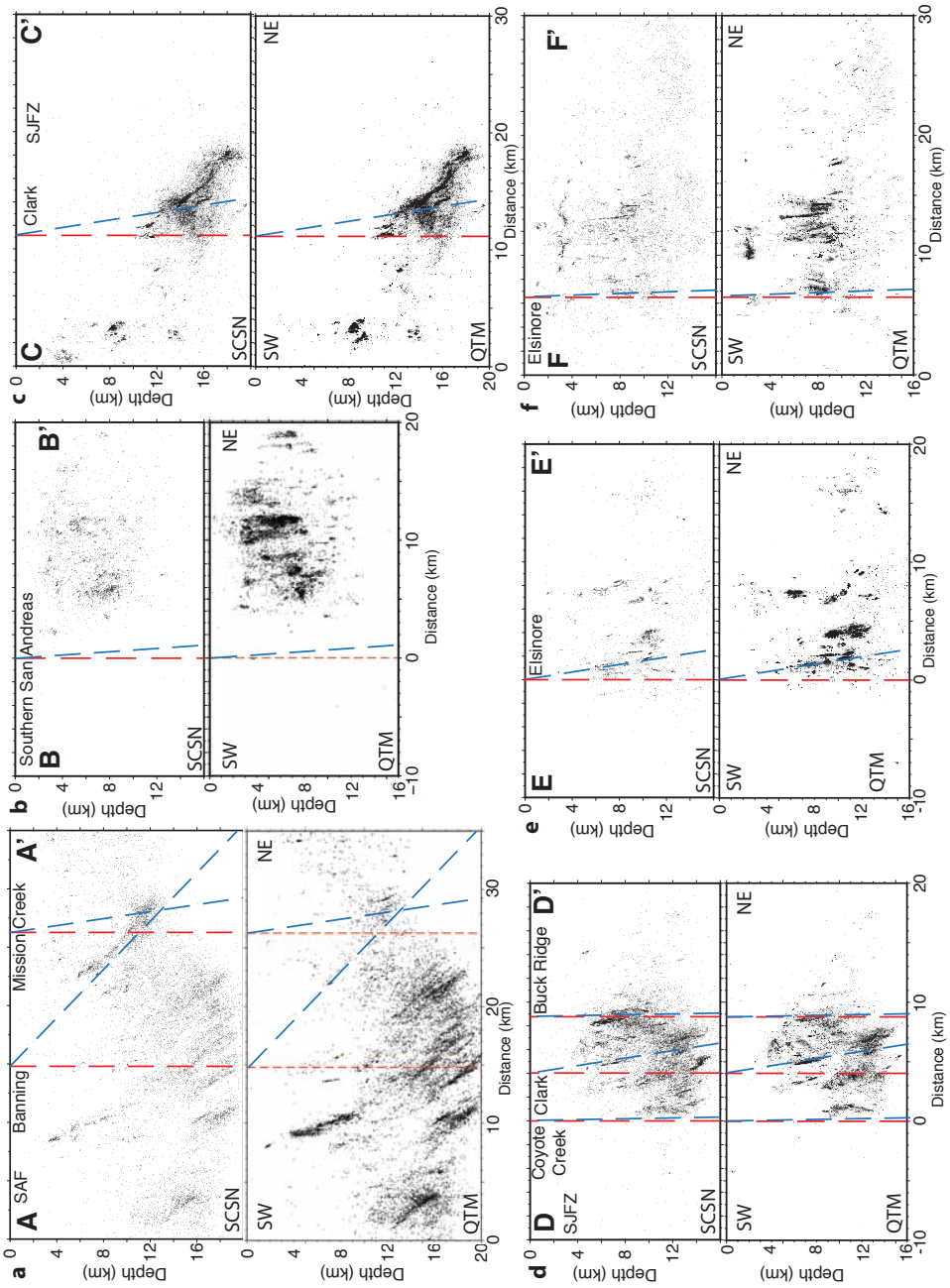

Figure 7. Seismicity profiles, locations marked in Figure 6. Each top subpanel shows locations from the 1981-2017 SCSN catalog, bottom from 2008-2017 QTM catalog. Red dashed lines in profiles show vertical projection of fault surface traces, blue dashed lines show average dips of each fault segment as listed in the SCEC CFM-5 model. There is no vertical exaggeration in the profiles so that any dip angles are true dips. Seismicity shown is from within 5 km of each respective profile.

ESSOAr | https://doi.org/10.1002/essoar.10502174.1 | Non-exclusive | First posted online: Fri, 7 Feb 2020 06:51:43 | This content has not been peer reviewed.

that the observations are related to a regional pattern. Preexisting NE-dipping extensional structures may have influenced the development of northeast dip on strike-slip faults (Dorsey et al., 2012; Mason et al., 2017; Shirvell et al., 2009).

4 Discussion: The importance of fault and fabric reactivation and inheritance

The current tectonic regime in Southern California is one of transform motion on the plate boundary and regional N-S compressive stress (Heidbach, Rajabi, Reiter, Ziegler, & WSM Team, 2016; Kreemer, Blewitt, & Klein, 2014; Yang & Hauksson, 2013). There is thrust faulting in the Western Transverse Ranges (Figure 4, bottom left) past the area of profile A to Cajon Pass (Figure 6. In other areas, strike-slip faulting dominates (Yang & Hauksson, 2013). The maximum compressive stress in the crust is generally N-S with some regional variations and rotations with depth (M.-G. P. Abolfathian N. & Ben-Zion, 2020; N. Abolfathian, Martinez-Garzon, & Ben-Zion, 2019). This suggests that microcracks in the brittle upper crust (above crack closure depths) would be expected to generally align N-S, parallel to the maximum compressive stress. Li and Peng (2017) analysed shear wave splitting from local events within the seismogenic portion in the crust in southern California. They found large deviations between the orientation of maximum compressive stress and the observed fast polarization orientation, with the latter rotating to fault-parallel along large parts of the San Andreas Fault, regions between the SJFZ and Elsinore Faults, the Western Transverse Ranges, and other areas. Li and Peng (2017) concluded that the signal from present-day compression was affected by older structural features generating anisotropy.

Our results extend their observations in two aspects. First, the fault-parallel anisotropy is not limited to the seismogenic crust, but extends through all lithospheric depths (Figure 4). Like the shallow results from Li and Peng (2017), the fault-parallel foliation is not limited to the vicinity of major faults but appears pervasive through the entire region. Second, rather than finding vertical foliation or horizontal lineation (i.e., an A_2 signal) and vertical fault traces as one may expect with Andersonian mechanics and a homogeneous crust under dominant transform deformation, our results show dominant dipping fabric and faults throughout the region. The strikes of the dominant fabric vary along with the fault strike by geological block. We interpret this as a regional fabric that is

ESSOAr | https://doi.org/10.1002/essoar.10502174.1 | Non-exclusive | First posted online: Fri, 7 Feb 2020 06:51:43 | This content has not been peer reviewed.

not controlled by a present-day region-wide deformation regime, but is dominated by inherited fabric stemming from the tectonic history of each block and of the entire region.

Much like the small-scale examples of inherited fabric and reactivation discussed by Dorsey et al. (2012) and Mason et al. (2017) in the case of the Elsinore and San Jacinto Faults influenced by the Western Salton Detachment Fault, preexisting fabric, fault structures, and shear zones from previous compressional and extensional regimes likely have had a controlling influence on the development and geometry of present-day transform faults across the region. Exhumed shear zones in the area show evidence for reactivation of Mesozoic thrusts in Cenozoic normal faulting (Goodwin & Wenk, 1995; Todd, Erskine, & Morton, 1988). Langenheim, Jachens, Morton, Kistler, and Matti (2004) propose that the geometry and path of the present-day San Jacinto Fault was dictated by a preexisting physical property contrast, and that earthquakes on the fault continue to nucleate along this discontinuity. Detailed seismic imaging studies show that the main strike-slip faults in Southern California are associated with prominent lithology contrasts (e.g. Fang et al., 2016; Qiu et al., 2019; Share & Ben-Zion, 2016, 2018; Share et al., 2019). Here, we take this concept of inheritance further and propose that the southern California region is permeated by a pervasive rock fabric throughout the lithosphere. Present-day faults and deformation align along strikes dictated by this inherited fabric, leading to geometries such as dipping strike-slip faults that would be energetically unfavorable in an isotropic homogeneous medium.

Figure 8 illustrates this concept with a loose tie to previous tectonic states and ages. A long history of compression in the Mesozoic and Cenozoic generated NE-dipping thrust fabric and faults (Figure 8, panel 1). The same structures were reactivated in normal faulting during extensional episodes in the Cretaceous and Miocene (Figure 8, panel 2). Miocene initiation of transform motion exploited the same NW-SW striking features and fabric, leading to dipping and listric strike-slip fault structures paralleling the inherited fabric (Figure 8, panel 3). We propose that present-day faulting and deformation are significantly affected by inherited structure. This observation has broad implications on the modeling and interpretation of present-day continental lithospheric deformation, faulting, and fault loading. To treat these processes accurately, it may be necessary to not only consider present-day stress, but also take into account preexisting fabric from past deformation. The pervasive nature of such fabric in southern California implies that rather than considering individual shear zones, it may be sufficient to impose a preferential fab-

ESSOAr | https://doi.org/10.1002/essoar.10502174.1 | Non-exclusive | First posted online: Fri, 7 Feb 2020 06:51:43 | This content has not been peer reviewed.

ric (i.e. anisotropy of viscosity) when modeling deformation processes on a lithospheric scale. More sophisticated models should also explore the effect of major rheological boundaries associated with the Peninsular Ranges batholith and the Orocopia, Pelona, and Rand schists.

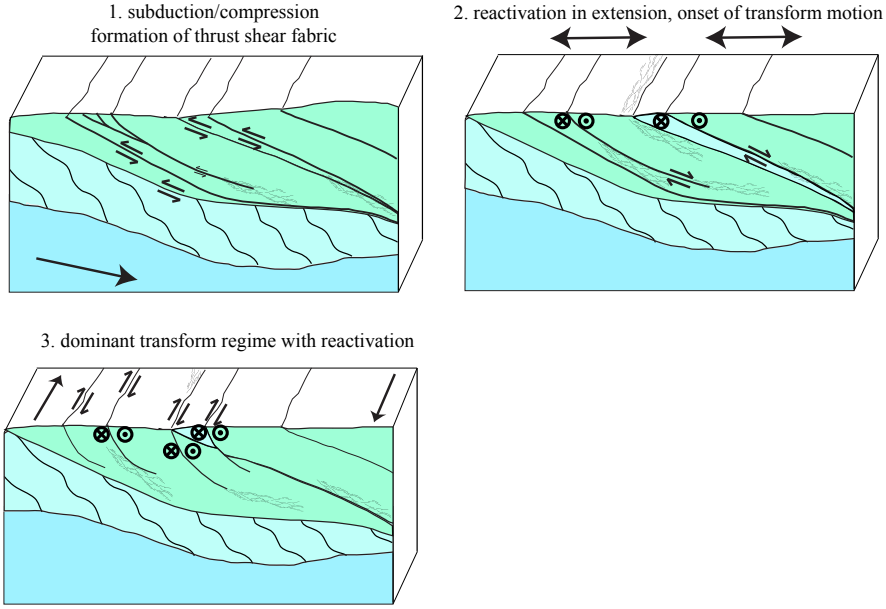

Figure 8. Conceptual illustration of the dominance of inherited structures and fabric on present-day tectonic fabric in Southern California. 1. Compressional regime during Farallon subduction (some reactivation of Mesozoic thrusts in extension). 2. Reactivation of compressional structures during extension; exhumation of some shear zones and deeper units; onset of transform deformation. 3. Dominant transform regime with dipping structures and fabric from the inherited compressional and extensional geometries. Location, strike, and dip of active structures in each regime are influenced by inherited prior structures and fabric.

5 Conclusions

We analyzed receiver functions for conversions from contrasts in dipping foliation and from dipping isotropic interfaces and found such contrasts to be pervasive through lithospheric depths and laterally pervasive in Southern California. The strike of dipping fabric and contrasts tends to parallel that of surface faults. Seismicity profiles perpen-

ESSOAr | https://doi.org/10.1002/essoar.10502174.1 | Non-exclusive | First posted online: Fri, 7 Feb 2020 06:51:43 | This content has not been peer reviewed.

dicular to major transform faults show dipping or listric features, with dips as well as damage zones preferentially to the northeast. The results are consistent with tomographic and fault zone head wave imaging studies.

If deformation in the lithosphere was controlled by present day processes, and if inherited fabric was reset, one may expect vertical strike-slip faults and deformation fabric that is strongest in the immediate vicinity of faults. We observe pervasive fabric that is not concentrated around faults and consistently dips to the northeast despite present day dominant strike-slip deformation. Taken together with local geological reconstructions and other observations showing reactivation of inherited deformation features, this leads us to propose that present-day deformation is to a large extent controlled by regional lithospheric fabrics inherited from past deformation episodes.

Acknowledgments

The facilities of the Southern California Earthquake Data Center (SCEDC) and of the IRIS Data Services (IRIS Data Management Center) were used for access to waveforms and related metadata used in this study. IRIS Data Services are funded through the Seismological Facilities for the Advancement of Geoscience and EarthScope (SAGE) Proposal of the National Science Foundation (NSF) under Cooperative Agreement EAR-1261681. The SCEDC and SCSN are funded through U.S. Geological Survey Grant G10 AP00091. This research was funded by NSF grants EAR 1927246, 1735890, 1251193, and 1841315, and by Southern California Earthquake Center (SCEC) grant 17097 (based on NSF Cooperative Agreement EAR-0529922 and USGS Cooperative Agreement 07HQAG0008). We thank P. Share for extracting 3-D velocity models, S. Marshall for providing fault summary data for the SCEC CFM-5.2, K. Mahan and M. Frothingham for discussions, and C. Condit for a basic sketch for Figure 8.

ESSOAr | https://doi.org/10.1002/essoar.10502174.1 | Non-exclusive | First posted online: Fri, 7 Feb 2020 06:51:43 | This content has not been peer reviewed.

References

Abolfathian, M.-G. P., N., & Ben-Zion, Y. (2020, MAR). Variations of stress parameters in the Southern California plate boundary around the South Central Transverse Ranges. *Seismological Research Letters - 2020 SSA meeting abstracts*, *?*(?), ?-?

Abolfathian, N., Martinez-Garzon, P., & Ben-Zion, Y. (2019, MAR). Spatiotemporal Variations of Stress and Strain Parameters in the San Jacinto Fault Zone. *Pure and Applied Geophysics*, *176*(3), 1145-1168. doi: 10.1007/s00024-018-2055-y

Atwater, T., & Stock, J. (1998, MAY). Pacific North America plate Tectonics of the Neogene southwestern United States: An update. *International Geology Review*, *40*(5), 375-402. doi: 10.1080/00206819809465216

Avouac, J.-P., Ayoub, F., Wei, S., Ampuero, J.-P., Meng, L., Leprince, S., ... Helmberger, D. (2014, APR 1). The 2013, Mw 7.7 Balochistan earthquake, energetic strike-slip reactivation of a thrust fault. *Earth and Planetary Science Letters*, *391*, 128-134. doi: 10.1016/j.epsl.2014.01.036

Barak, S., Klemperer, S. L., & Lawrence, J. F. (2015, NOV). San Andreas Fault dip, Peninsular Ranges mafic lower crust and partial melt in the Salton Trough, Southern California, from ambient-noise tomography. *Geochemistry Geophysics Geosystems*, *16*(11), 3946-3972. doi: 10.1002/2015GC005970

Becken, M., Ritter, O., Bedrosian, P. A., & Weckmann, U. (2011, DEC 1). Correlation between deep fluids, tremor and creep along the central San Andreas fault. *Nature*, *480*(7375), 87-U248. doi: 10.1038/Nature10609

Bernard, R. E., & Behr, W. M. (2017, JUL). Fabric heterogeneity in the Mojave lower crust and lithospheric mantle in Southern California. *Journal of Geophysical Research*, *122*(7), 5000-5025. doi: 10.1002/2017JB014280

Bianchi, I., Park, J., Agostinetti, N. P., & Levin, V. (2010, DEC 18). Mapping seismic anisotropy using harmonic decomposition of receiver functions: An application to Northern Apennines, Italy. *Journal of Geophysical Research - Solid Earth*, *115*. doi: 10.1029/2009JB007061

Bianchi, I., Piana Agostinetti, N., De Gori, P., & Chiarabba, C. (2008). Deep structure of the colli albani volcanic district (central italy) from receiver functions analysis. *Journal of Geophysical Research: Solid Earth*, *113*(B9). Retrieved from `https://agupubs.onlinelibrary.wiley.com/doi/abs/`

ESSOAr | https://doi.org/10.1002/essoar.10502174.1 | Non-exclusive | First posted online: Fri, 7 Feb 2020 06:51:43 | This content has not been peer reviewed.

10.1029/2007JB005548 doi: 10.1029/2007JB005548

Bourne, S., England, P., & Parsons, B. (1998, FEB 12). The motion of crustal blocks driven by flow of the lower lithosphere and implications for slip rates of continental strike-slip faults. *Nature*, *391*(6668), 655-659. doi: 10.1038/35556

Brownlee, S. J., Schulte-Pelkum, V., Raju, A., Mahan, K., Condit, C., & Orlandini, O. F. (2017, SEP). Characteristics of deep crustal seismic anisotropy from a compilation of rock elasticity tensors and their expression in receiver functions. *Tectonics*, *36*(9), 1835-1857. doi: 10.1002/2017TC004625

Dair, L., & Cooke, M. L. (2009, FEB). San Andreas fault geometry through the San Gorgonio Pass, California. *Geology*, *37*(2), 119-122. doi: 10.1130/G25101A.1

Dolan, J. F., Bowman, D. D., & Sammis, C. G. (2007, SEP). Long-range and long-term fault interactions in Southern California. *Geology*, *35*(9), 855-858. doi: 10.1130/G23789A.1

Dorsey, R. J., Axen, G. J., Peryam, T. C., & Kairouz, M. E. (2012, MAR 16). Initiation of the Southern Elsinore Fault at similar to 1.2 Ma: Evidence from the Fish Creek-Vallecito Basin, southern California. *Tectonics*, *31*. doi: 10.1029/2011TC003009

Doser, D. I., & Kanamori, H. (1986). Depth of seismicity in the Imperial Valley region (1977â1983) and its relationship to heat flow, crustal structure and the October 15, 1979, earthquake. *Journal of Geophysical Research: Solid Earth*, *91*(B1), 675–688.

England, P., & Jackson, J. (1989). Active deformation of the continents. *Annual Review of Earth and Planetary Sciences*, *17*, 197-226. doi: 10.1146/annurev.earth.17.1.197

Fang, H., Zhang, H., Yao, H., Allam, A., Zigone, D., Ben-Zion, Y., ... van der Hilst, R. D. (2016, MAY). A new algorithm for three-dimensional joint inversion of body wave and surface wave data and its application to the Southern California plate boundary region. *Journal of Geophysical Research-Solid Earth*, *121*(5), 3557-3569. doi: 10.1002/2015JB012702

Fialko, Y. (2006, JUN 22). Interseismic strain accumulation and the earthquake potential on the southern San Andreas fault system. *Nature*, *441*(7096), 968-971. doi: 10.1038/nature04797

Forand, D., Evans, J. P., Janecke, S. U., & Jacobs, J. (2018, JAN). Insights into

ESSOAr | https://doi.org/10.1002/essoar.10502174.1 | Non-exclusive | First posted online: Fri, 7 Feb 2020 06:51:43 | This content has not been peer reviewed.

529 fault processes and the geometry of the San Andreas fault system: Analysis of
530 core from the deep drill hole at Cajon Pass, California. *Geological Society of*
531 *America Bulletin*, *130*(1-2), 64-92. doi: 10.1130/B31681.1
532 Fossen, H., & Cavalcante, G. C. G. (2017, AUG). Shear zones - A review. *Earth-*
533 *Science Reviews*, *171*, 434-455. doi: 10.1016/j.earscirev.2017.05.002
534 Fuis, G. S., Bauer, K., Goldman, M. R., Ryberg, T., Langenheim, V. E., Scheirer,
535 D. S., ... Aagaard, B. (2017, AUG). Subsurface Geometry of the San Andreas
536 Fault in Southern California: Results from the Salton Seismic Imaging Project
537 (SSIP) and Strong Ground Motion Expectations. *Bulletin of the Seismological*
538 *Society of America*, *107*(4), 1642-1662. doi: {10.1785/0120160309}
539 Fuis, G. S., Scheirer, D. S., Langenheim, V. E., & Kohler, M. D. (2012, FEB).
540 A New Perspective on the Geometry of the San Andreas Fault in Southern
541 California and Its Relationship to Lithospheric Structure. *Bulletin of the*
542 *Seismological Society of America*, *102*(1), 236-251. doi: 10.1785/0120110041
543 Goodwin, L., & Wenk, H. (1995, MAY). Development of phyllonite from
544 granodiorite - mechanisms of grain-size reduction in the Santa-Rosa my-
545 lonite zone, California. *Journal of Structural Geology*, *17*(5), 689-&. doi:
546 10.1016/0191-8141(94)00093-F
547 Harms, T. A., Brady, J. B., Burger, H. R., & Cheney, J. T. (2004). advances in the
548 geology of the tobacco root mountains, montana,and their implications for the
549 history of the northern wyoming province.
550 Hauksson, E., & Meier, M. (2019). Applying Depth Distribution of Seismicity to De-
551 termine Thermo-Mechanical Properties of the Seismogenic Crust in Southern
552 California: Comparing Lithotectonic Blocks). *Pure and Applied Geophysics*,
553 *176*, 1061–1081. doi: 10.1007/s00024-018-1981-z
554 Hauksson, E., Yang, W., & Shearer, P. M. (2012, OCT). Waveform Relocated
555 Earthquake Catalog for Southern California (1981 to June 2011). *Bul-*
556 *letin of the Seismological Society of America*, *102*(5), 2239-2244. doi:
557 10.1785/0120120010
558 Heidbach, O., Rajabi, M., Reiter, K., Ziegler, M., & WSM Team, x. (2016). World
559 Stress Map Database Release 2016. *GFZ Data Services*, 1061–1081. doi: 10
560 .5880/WSM.2016.001
561 Johnson, K. M., Shelly, D. R., & Bradley, A. M. (2013). Simulations of tremor-

ESSOAr | https://doi.org/10.1002/essoar.10502174.1 | Non-exclusive | First posted online: Fri, 7 Feb 2020 06:51:43 | This content has not been peer reviewed.

related creep reveal a weak crustal root of the San Andreas Fault. *Geophysical Research Letters*, *40*(7), 1300-1305. Retrieved from `https://agupubs.onlinelibrary.wiley.com/doi/abs/10.1002/grl.50216` doi: 10.1002/grl.50216

Jones, C., & Phinney, R. (1998). Seismic structure of the lithosphere from teleseismic converted arrivals observed at small arrays in the southern Sierra Nevada and vicinity, California. *Journal of Geophysical Research*, *103*, 10,065-10,090.

Jones, L., Hutton, L., Given, D., & Allen, C. (1986, DEC). The July 1986 north Palm-Springs, California, earthquake - the north Palm-Springs, California, earthquake sequence of July 1986. *Bulletin of the Seismological Society of America*, *76*(6), 1830-1837.

Kreemer, C., Blewitt, G., & Klein, E. C. (2014, OCT). A geodetic plate motion and Global Strain Rate Model. *Geochemistry Geophysics Geosystems*, *15*(10), 3849-3889. doi: 10.1002/2014GC005407

Langenheim, V., Jachens, R., Morton, D., Kistler, R., & Matti, J. (2004, SEP-OCT). Geophysical and isotopic mapping of preexisting crustal structures that influenced the location and development of the San Jacinto fault zone, southern California. *Geological Society of America Bulletin*, *116*(9-10), 1143-1157. doi: 10.1130/B25277.1

Levin, V., & Park, J. (1998). $P - SH$ conversions in layered media with hexagonally symmetric anisotropy: A cookbook. *Pure and Applied Geophysics*, *151*, 669-697.

Li, Z., & Peng, Z. (2017, OCT 16). Stress- and Structure-Induced Anisotropy in Southern California From Two Decades of Shear Wave Splitting Measurements. *Geophysical Research Letters*, *44*(19), 9607-9614. doi: 10.1002/2017GL075163

Ligorria, J., & Ammon, C. (1999, OCT). Iterative deconvolution and receiver-function estimation. *Bulletin of the Seismological Society of America*, *89*(5), 1395-1400.

Lin, F. C., Ritzwoller, M. H., Yang, Y., Moschetti, M. P., & Fouch, M. J. (2011). Complex and variable crustal and uppermost mantle seismic anisotropy in the western United States. *Nature Geosci.*, *4*, 55–61. doi: 10.1038/NGEO1036

Lindsey, E. O., & Fialko, Y. (2013, FEB). Geodetic slip rates in the southern

ESSOAr | https://doi.org/10.1002/essoar.10502174.1 | Non-exclusive | First posted online: Fri, 7 Feb 2020 06:51:43 | This content has not been peer reviewed.

595 San Andreas Fault system: Effects of elastic heterogeneity and fault geom-
596 etry. *Journal of Geophysical Research-Solid Earth*, *118*(2), 689-697. doi:
597 10.1029/2012JB009358

598 Liu, Z., & Park, J. (2017, MAR). Seismic receiver function interpretation: Ps split-
599 ting or anisotropic underplating? *Geophysical Journal International*, *208*(3),
600 1332-1341. doi: 10.1093/gji/ggw455

601 Long, M. D., Ford, H. A., Abrahams, L., & Wirth, E. A. (2017, DEC). The seis-
602 mic signature of lithospheric deformation beneath eastern North America due
603 to Grenville and Appalachian orogenesis. *Lithosphere*, *9*(6), 987-1001. doi:
604 10.1130/L660.1

605 Mason, C. C., Spotila, J. A., Axen, G., Dorsey, R. J., Luther, A., & Stockli, D. F.
606 (2017, DEC). Two-Phase Exhumation of the Santa Rosa Mountains: Low-
607 and High-Angle Normal Faulting During Initiation and Evolution of the
608 Southern San Andreas Fault System. *Tectonics*, *36*(12), 2863-2881. doi:
609 10.1002/2017TC004498

610 Montési, L. G. J. (2004). Controls of shear zone rheology and tectonic loading on
611 postseismic creep. *Journal of Geophysical Research-Solid Earth*, *109*(B10).
612 Retrieved from `https://agupubs.onlinelibrary.wiley.com/doi/abs/`
613 `10.1029/2003JB002925` doi: 10.1029/2003JB002925

614 Murphy, J. M., Fuis, G. S., Ryberg, T., Lutter, W. J., Catchings, R. D., & Gold-
615 man, M. R. (2010, DEC). Detailed P- and S- Wave Velocity Models along the
616 LARSE II Transect, Southern California. *Bulletin of the Seismological Society*
617 *of America*, *100*(6), 3194-3212. doi: 10.1785/0120090004

618 Nadeau, R., & Dolenc, D. (2005, JAN 21). Nonvolcanic tremors deep beneath the
619 San Andreas Fault. *Science*, *307*(5708), 389. doi: 10.1126/Science.1107142

620 Oglesby, D., Archuleta, R., & Nielsen, S. (2000, JUN). The three-dimensional dy-
621 namics of dipping faults. *Bulletin of the Seismological Society of America*,
622 *90*(3), 616-628. doi: 10.1785/0119990113

623 Ozacar, A. A., & Zandt, G. (2009, AUG). Crustal structure and seismic anisotropy
624 near the San Andreas Fault at Parkfield, California. *Geophysical Journal Inter-*
625 *national*, *178*(2), 1098-1104. doi: 10.1111/j.1365-246X.2009.04198.x

626 Park, J., & Levin, V. (2016, NOV). Anisotropic shear zones revealed by backaz-
627 imuthal harmonics of teleseismic receiver functions. *Geophysical Journal Inter-*

ESSOAr | https://doi.org/10.1002/essoar.10502174.1 | Non-exclusive | First posted online: Fri, 7 Feb 2020 06:51:43 | This content has not been peer reviewed.

national, *207*(2), 1216-1243. doi: 10.1093/gji/ggw323

Platt, J. P., & Becker, T. W. (2010). Where is the real transform boundary in California? *Geochemistry Geophysics Geosystems*, *11*(Q06013). doi: 10.1029/2010GC003060

Plesch, A., Shaw, J. H., Benson, C., Bryant, W. A., Carena, S., Cooke, M., ... Yeats, R. (2007, DEC). Community fault model (CFM) for southern California. *Bulletin of the Seismological Society of America*, *97*(6), 1793-1802. doi: 10.1785/0120050211

Porter, R., Zandt, G., & McQuarrie, N. (2011, JUN). Pervasive lower-crustal seismic anisotropy in Southern California: Evidence for underplated schists and active Tectonics. *Lithosphere*, *3*(3), 201-220. doi: 10.1130/L126.1

Qiu, H., Lin, F.-C., & Ben-Zion, Y. (2019, SEP). Eikonal Tomography of the Southern California Plate Boundary Region. *Journal of Geophysical Research-Solid Earth*, *124*(9), 9755-9779. doi: 10.1029/2019JB017806

Richter, C. F., Allen, C., & Nordquist, J. (1958). The desert hot springs earthquakes and their tectonic environment. *Bulletin of the Seismological Society of America*, *48*(4), 315–337.

Ross, Z. E., Hauksson, E., & Ben-Zion, Y. (2017, MAR). Abundant off-fault seismicity and orthogonal structures in the San Jacinto fault zone. *Science Advances*, *3*(3). doi: 10.1126/sciadv.1601946

Ross, Z. E., Trugman, D. T., Hauksson, E., & Shearer, P. M. (2019, MAY 24). Searching for hidden earthquakes in Southern California. *Science*, *364*(6442), 767+. doi: 10.1126/science.aaw6888

Roy, M., & Royden, L. (2000a, MAR 10). Crustal rheology and faulting at strike-slip plate boundaries 1. An analytic model. *Journal of Geophysical Research-Solid Earth*, *105*(B3), 5583-5597. doi: 10.1029/1999JB900339

Roy, M., & Royden, L. (2000b, MAR 10). Crustal rheology and faulting at strike-slip plate boundaries 2. Effects of lower crustal flow. *Journal of Geophysical Research-Solid Earth*, *105*(B3), 5599-5613. doi: 10.1029/1999JB900340

Ryberg, T., Haberland, C., Fuis, G. S., Ellsworth, W. L., & Shelly, D. R. (2010, DEC). Locating non-volcanic tremor along the San Andreas Fault using a multiple array source imaging technique. *Geophysical Journal International*, *183*(3), 1485-1500. doi: {10.1111/j.1365-246X.2010.04805.x}

ESSOAr | https://doi.org/10.1002/essoar.10502174.1 | Non-exclusive | First posted online: Fri, 7 Feb 2020 06:51:43 | This content has not been peer reviewed.

Sato, H., Kato, N., Abe, S., Van Horne, A., & Takeda, T. (2015, MAR 16). Reactivation of an old plate interface as a strike-slip fault in a slip-partitioned system: Median Tectonic Line, SW Japan. *Tectonophysics*, *644*, 58-67. doi: 10.1016/j.tecto.2014.12.020

Savage, M. K. (1998). Lower crustal anisotropy or dipping boundaries: Effects on receiver functions and a case study in New Zealand. *Journal of Geophysical Research*, *103*, 15,069-15,087.

Schulte-Pelkum, V., & Mahan, K. H. (2014a, NOV). Imaging Faults and Shear Zones Using Receiver Functions. *Pure and Applied Geophysics*, *171*(11), 2967-2991. doi: 10.1007/s00024-014-0853-4

Schulte-Pelkum, V., & Mahan, K. H. (2014b, SEP 15). A method for mapping crustal deformation and anisotropy with receiver functions and first results from USArray. *Earth and Planetary Science Letters*, *402*(SI), 221-233. doi: 10.1016/j.epsl.2014.01.050

Share, P.-E., & Ben-Zion, Y. (2016, OCT 28). Bimaterial interfaces in the south San Andreas Fault with opposite velocity contrasts NW and SE from San Gorgonio Pass. *Geophysical Research Letters*, *43*(20), 10680-10687. doi: {10.1002/2016GL070774}

Share, P.-E., & Ben-Zion, Y. (2018, NOV 16). A Bimaterial Interface Along the Northern San Jacinto Fault Through Cajon Pass. *Geophysical Research Letters*, *45*(21), 11622-11631. doi: {10.1029/2018GL079834}

Share, P.-E., Guo, H., Thurber, C. H., Zhang, H., & Ben-Zion, Y. (2019, MAR). Seismic Imaging of the Southern California Plate Boundary around the South-Central Transverse Ranges Using Double-Difference Tomography. *Pure and Applied Geophysics*, *176*(3), 1117-1143. doi: 10.1007/s00024-018-2042-3

Shaw, J. H., Plesch, A., Tape, C., Suess, M. P., Jordan, T. H., Ely, G., ... Munster, J. (2015, APR 1). Unified Structural Representation of the southern California crust and upper mantle. *Earth and Planetary Science Letters*, *415*, 1-15. doi: {10.1016/j.epsl.2015.01.016}

Shelly, D. R. (2017, MAY). A 15-year catalog of more than 1 million low-frequency earthquakes: Tracking tremor and slip along the deep San Andreas Fault. *Journal of Geophysical Research - Solid Earth*, *122*(5), 3739-3753. doi: {10.1002/2017JB014047}

ESSOAr | https://doi.org/10.1002/essoar.10502174.1 | Non-exclusive | First posted online: Fri, 7 Feb 2020 06:51:43 | This content has not been peer reviewed.

694 Shelly, D. R., & Hardebeck, J. L. (n.d.). Precise tremor source locations and ampli-
695 tude variations along the lower-crustal central San Andreas Fault. *Geophysical*
696 *Research Letters*.

697 Shinevar, W. J., Behn, M. D., Hirth, G., & Jagoutz, O. (2018, JUL 15). Infer-
698 ring crustal viscosity from seismic velocity: Application to the lower crust of
699 Southern California. *Earth and Planetary Science Letters*, *494*, 83-91. doi:
700 10.1016/j.epsl.2018.04.055

701 Shirvell, C. R., Stockli, D. F., Axen, G. J., & Grove, M. (2009, MAR 24). Miocene-
702 Pliocene exhumation along the west Salton detachment fault, southern Califor-
703 nia, from (U-Th)/He thermochronometry of apatite and zircon. *Tectonics*, *28*.
704 doi: 10.1029/2007TC002172

705 Sibson, R. (1983). Continental fault structure and the shallow earthquake source.
706 *Journal of the Geological Society*, *140*(SEP), 741-767. doi: 10.1144/gsjgs.140.5
707 .0741

708 Titus, S. J., Medaris, L. G., Jr., Wang, H. F., & Tikoff, B. (2007). Continuation
709 of the San Andreas fault system into the upper mantle: Evidence from spinel
710 peridotite xenoliths in the Coyote Lake basalt, central California. *Tectono-*
711 *physics*, *429*(1-2), 1-20. doi: 10.1016/j.tecto.2006.07.004

712 Todd, V. R., Erskine, B. G., & Morton, D. M. (1988). Metamorphic and tectonic
713 evolution of the northern Peninsular Ranges batholith, southern California.
714 In W. G. Ernst (Ed.), *Metamorphic and Crustal Evolution of the Northern*
715 *Peninsular Ranges Batholith, southern California, Rubey Volume no. VIII.*
716 Englewood Cliffs, New Jersey: Prentice-Hall.

717 Vauchez, A., Tommasi, A., & Mainprice, D. (2012). Faults (shear zones) in the
718 Earth's mantle. *Tectonophysics*, *558*, 1–27.

719 Vergne, J., Wittlinger, G., Farra, V., & Su, H. (2003). Evidence for upper crustal
720 anisotropy in the songpan-ganze (northeastern tibet) terrane. *Geophysical*
721 *Research Letters*, *30*(11). Retrieved from `https://agupubs.onlinelibrary`
722 `.wiley.com/doi/abs/10.1029/2002GL016847` doi: 10.1029/2002GL016847

723 Yang, W., & Hauksson, E. (2013, JUL). The tectonic crustal stress field and
724 style of faulting along the Pacific North America Plate boundary in South-
725 ern California. *Geophysical Journal International*, *194*(1), 100-117. doi:
726 10.1093/gji/ggt113

ESSOAr | https://doi.org/10.1002/essoar.10502174.1 | Non-exclusive | First posted online: Fri, 7 Feb 2020 06:51:43 | This content has not been peer reviewed.

Zandt, G., Gilbert, H., Owens, T., Ducea, M., Saleeby, J., & Jones, C. (2004, SEP 2). Active foundering of a continental arc root beneath the southern Sierra Nevada in California. *Nature*, *431*(7004), 41-46. doi: 10.1038/nature02847

Zhu, L. (2002). Deformation in the lower crust and downward extent of the San Andreas Fault as revealed by teleseismic waveforms. *Earth Planets and Space*, *54*(11), 1005-1010. (International Symposium on Slip and Flow Processes in and Below the Seismogenic Region, SENDAI, JAPAN, NOV 05-08, 2001) doi: 10.1186/BF03353293